# Structure of the type VI secretion system protein VgrS from *Salmonella* Typhimurium

Kartik Sachar[*], Matthew Van Schepdael[*], Karsen L. Winters, and Gerd Prehna[#]

Department of Microbiology, University of Manitoba, Winnipeg, MB, R3T 2N2, Canada

[*] Indicates equal author contribution

**Keywords:**
Type VI secretion system, VgrG, *Salmonella* Typhimurium, bacterial warfare, X-ray Crystallography.

[#]To whom correspondence should be addressed: GP
Email:gerd.prehna@umanitoba.ca

**SUMMARY**

Enteric bacterial pathogens employ various strategies to colonize the intestine and cause diseases ranging from gastroenteritis to systemic infections. For example, *Salmonella enterica* utilizes a nanomachine known as the type VI secretion system (T6SS) to facilitate colonization of the host gut. However, the varied mechanistic details of how the T6SS is loaded with effector proteins remains to be elucidated. Here, we present an X-ray crystal structure of the *Salmonella* Typhimurium VgrG (VgrS) that serves as platform for T6SS effector loading. Compared to other known structures of VgrG proteins, the VgrS trimer adopts an alternative open conformation composed of a domain-swap between the monomers in the gp27 region. Additionally, a comparative structural analysis of VgrS with other VgrG proteins reveals molecular variations that may contribute to specific effector loading mechanisms. Our structural data and molecular analysis highlight the observation that the T6SS of each bacterial species or strain is unique.

## INTRODUCTION

Bacterial antagonism and the competition for essential nutrients and space is a primary factor that shapes microbial community structure and dynamics. Consequently, bacteria have developed sophisticated multi-protein nanomachinery to engage in interspecies competition and eliminate rival bacteria. *Salmonella enterica*, a major cause of human gastroenteritis, employs such a competition mechanism named the type VI secretion system (T6SS)[1–3]. The T6SS is a dynamic nanomachine that Gram-negative bacteria used to inject toxic effectors to kill rival bacteria in a contact-dependent manner[4]. *S. enterica* encodes several T6SS across different *Salmonella* Pathogenicity Islands (SPIs) and serovars [3,5]. However, each *S. enterica* subtype and serovar has unique T6SS molecular adaptations that result in different clinical manifestations and host specificity[3,5].

The current T6SS model includes 13 core proteins (TssA-M, *Pseudomonas* nomenclature), divided into three components: a membrane-anchoring complex, a phage tail-like structure, and a baseplate complex[6]. The membrane-anchoring complex secures the apparatus to the bacterial membranes, while the baseplate acts as a scaffold for assembling the tail-like structure[7–11]. The phage tail-like structure functions as the site for effector recruitment and consists of four proteins: TssB, TssC, Hcp, and VgrG[12,13]. The TssBC proteins form a sheath that assembles around the homo-hexameric Hcp tube. Upon full extension of the tail, the TssBC sheath contracts[14]. This propels the Hcp tube, VgrG, and their bound effectors into an adjacent cell[13].

The primary function of the T6SS is to secrete protein effectors, which exert diverse toxic effects on the targeted prey cell[15]. A critical step before secretion is the assembly and loading of effectors onto the T6SS apparatus. There is no singular structural feature that defines T6SS effector loading, with effectors often associating with the protein VgrG that forms the T6SS puncturing tip[16–21]. VgrG proteins can be covalently linked to an effector, or effectors can be non-covalently loaded onto VgrG by the use of adaptors and chaperones[16,22–25]. For example, some effectors require cone-shaped adaptor domains termed PAAR or 'PAAR-like', which bind the top of the VgrG β-prism and are said to 'sharpen' the T6SS[26–28]. PAAR domains can also require a chaperone for loading, such as Eags (DUF1795), that load membrane protein effectors onto VgrG[23]. Furthermore, different VgrG proteins can have unique structural modifications that serve

to recruit adaptors. Namely, adaptors such as Tap(DUF4123) recognize a helix-turn-helix extension in their cognate VgrG to load diverse effectors[29]. Additionally, VgrG can be extended by adaptor domains such as transthyretin-like (TTR) to recognize effectors[16,30]. Regardless of mechanism, what is apparent is that VgrG serves as universal but modular platform for effector loading.

Given the extensive variations in effector loading, detailed molecular data is required to understand how proteins associate with the T6SS apparatus. As VgrG is a modular central platform, each VgrG provides insight into molecular adaptions for species-specific effector secretion. In the case of *Salmonella* Typhimurium, it only encodes one VgrG, but has a diverse set of several effectors that must be loaded for secretion[1,31,32]. As such, the mechanism by which multiple different effectors are loaded onto the Salmonella T6SS for secretion remains unclear.

To help address the questions of effector loading, we have solved an X-ray crystal structure of the *Salmonella* Typhimurium VgrG named VgrS (STM0289)[1,3,33]. The VgrS crystal structure reported here shows an alternative open conformation relative to other VgrG proteins and reveals molecular features likely unique to *S.* Typhimurium T6SS effector loading. Our data further highlights that each T6SS is unique and specifically modified for the needs of each bacterial species.

## RESULTS

### Genetic context of VgrS in *Salmonella spp.*

VgrS is encoded within Salmonella Pathogenicity Island-6 (SPI-6), which houses all core T6SS genes[1,3,5,33], and four known effector/immunity pairs: *tae4/taiA, tlde1a/tldi1a*, *rhs1/rhsI1*, and *rhs2/sciX* (Figure 1A)[1,2,32,34]. Among these effectors, only the PAAR-containing Rhs1 has a defined mechanism for loading onto VgrS[23,35]. Furthermore, when compared to other *Salmonella* serovar T6SSs the genetic organization of the SPI-6 T6SS shows variability, especially among the repertoire of effectors (Figure S1A)[3]. The VgrS from *S.* Typhimurium and *S.* Typhi appear closely related but diverge in sequence from *S.* Gallinarum and *S.* Dubin, which contain a gp5 extension absent in both *S.* Typhimurium and *S.* Typhi (Figure S1B). Interestingly, *S.* Typhimurium and *S.* Typhi are major human pathogens whereas *S.* Gallinarium and *S.* Dubin appear adapted for chickens and

cattle[1,3,36,37]. Given this, we hypothesized that each VgrS must have unique molecular features to facilitate serovar-specific effector loading. As such, we pursued an experimental structure of VgrS to observe potential structural adaptations related to secretion.

**X-ray crystal structure of *S.* Typhimurium VgrS**

Full-length VgrS produced insoluble material, but a truncated construct (residues 81-729) that removed a region of predicted disorder was both soluble and purifiable[38,39]. Diffracting crystals of VgrS (81-729) were obtained and the structure of VgrS was solved by molecular replacement to a resolution of 3.1Å using a previous solved model of VgrG from *Pseudomonas aeruginosa* (PDB: 6H3L)[17] (Figure 1B and Table 1). The data can be processed as $P6_322$ with a VgrS monomer as the asymmetric unit. However, the lower symmetry space group $C222_1$ was chosen for refinement to have the biologically relevant VgrS trimer as the asymmetric unit (Figure S2A). The lower symmetry was also chosen as the interior of the trimer exhibited clear ligand density coordinated by each monomer (Figure S2B). In the crystal, the VgrS trimers pack tip-to-tip via their β-helix neck regions and the base of each trimer packs with the base (gp27 head) of a 2-fold rotated symmetry mate (Figure S2A). Strikingly, the resulting crystal packing features a rarely observed extremely high solvent content (82.22%), with a Mathews Coefficient of 6.91.

Similar to other VgrG proteins, the VgrS is a trimer composed of domains that are structurally homologous to the T4 bacteriophage spike-protein[40]. These domains include the head (gp27, residues 122 - 429), an OB-fold domain containing neck (residues 453-544), and the spike (gp5, residues 483 - 548) (Figure 1B)[16,20,21,35,40]. Additionally, VgrS has the general VgrG structure. This includes a hollow base (gp27 head), and a spike made of a triple-stranded β-helix (alternating strands from each monomer) including an interleaved β-prism (Figure 1B). The spike creates a flat triangular platform atop VgrS of ~33 Å per side that serves as the binding site for PAAR domain containing effectors[18,23,26,35].

Despite these similarities, the structure of VgrS diverges from other known VgrGs. The first notable difference is that VgrS contains a domain swap between each monomer (Figure 1B and Figure 2). Additionally, the gp27 head domain cup-like structure of VgrS

has a larger cavity than other VgrG proteins. The VgrS gp27 head measures approximately ~54 Å at the base and tapers to about ~17 Å near the top (triangular dimensions) (Figure 1B and Figure 2A, bottom views). This region of VgrG binds to the hexameric Hcp proteins of the T6SS tail. This raises the question of how VgrS recognizes Hcp proteins as compared to other VgrGs. Next, the VgrS platform contains a C-terminal tail extension (residues 711-729) that is approximately 31Å and notably shorter than extensions found in other VgrGs (Figure 1B and Figure 2A)[16,17]. In particular, the molecular features of C-terminal extensions have been implicated in many T6SS effector loading mechanisms[22,24,29,41,42], suggesting a unique mode of VgrS effector loading.

**VgrS contains multiple ligand coordination sites**

During building, we observed areas of density that could not be modelled by water and are likely ligands. Several sites were located at the β-helix midpoint (exterior and interior) as well as at the midpoint of the trimer on the inside of the gp27 cup (Figure S2B). Given that VgrS crystallized in high concentrations of ammonium sulfate (1.5M), the exterior ligands could be explained by sulfate ions. However, the central density coordinated by all three monomers with residues R620 and K622 could not be initially identified. Similar density was observed in VgrG1 (PDB: 4UHV), and VgrG1 (PDB: 4MTK) from *Pseudomonas aeruginosa* (Figure S2B)[20]. The internal density for 4UHV was not unmodelled, but for 4MTK the density was modelled as sulfate in part due to the crystallization conditions (1.4M $LiSO_4$). This suggests that VgrS also contains an internal sulfate.

Notably, phage proteins related to VgrG are known to contain metals[26]. As such, we performed inductively coupled plasma mass-spectrometry (ICP-MS) to help determine the identity of the bound ligands. We used the Eag chaperone SciW as a negative control as it does not bind metals and the zinc-containing papain-like protease from SARS-CoV-2 (PLpro) as a positive control[23,43,44]. ICP-MS results showed no significant enrichment of any tested metal ions in VgrS compared to the negative control (Figure S2C). Based on these results, the structure of the VgrS β-helix is stabilized by an internal anion such as sulfate. However, other anions such as chloride can also be modelled into the density

(Figure S2D). Overall, coordination of an internal anion by each monomer of the β-helix appears to be a conserved feature of VgrG proteins.

**The VgrS head domain adopts an open conformation**

A previous crystal structure of VgrG from *Pseudomonas aeruginosa* (PDB: 4UHV) shows that the head domain of VgrG1 can exist in two states, an "open" and "closed" conformation (Figure 2A)[20]. In the open conformation, the cavity at the base of the head domain widens due to the movement of loops at the very base of VgrG. This in turn creates an uneven spike top and loop-flip, which is unfavourable for PAAR binding (Figure 2A, right). In contrast, the three chains of the VgrS trimer in our structure have identical conformations (r.m.s.d of 0.235 $Å^2$) (Figure 2A). Comparing the VgrG1 open and closed conformations to VgrS, they align within the neck and spike (OB-fold and gp5) but differ in the gp27 base. This is especially pronounced at both the VgrS domain swap and in the conformations of the open/closed loops at the base (Figure 2B). VgrS differs from both the open and closed versions of VgrG1, with the comparison to the open VgrG1 highlighted. These differences also appear true for VgrS compared to all known VgrG structures (Figure S3A).

Instead of folding into anti-parallel β-strands as observed in other VgrG structures (Figure S3A), VgrS residues 319 to 366 (VgrG1 residues 220 to 264) form a loop that domain-swaps into the neighboring monomer. This makes all three monomers 'grasp' each other around the base of the trimer (Figure 1B and Figure 2B). A Fo-Fc difference map is shown in Figure S2E demonstrating the position and clear density for the domain swap. Of note, VgrS residues A345 to E356 could not be modeled due to insufficient electron density likely indicating flexibility. It is important to note that we cannot rule out that the missing density is due to cleavage or degradation during crystallization. Furthermore, it is also possible that the observed conformation could be due to the rare crystal packing of VgrS (Figure S2A). However, given that the conformation of the domain swap was the same in all three VgrS monomers, with the exact same portion of unmodelled residues, the observed conformation is unlikely to be due to non-specific cleavage, degradation, or crystal packing. Overall, the domain swap between the monomers results in a broader base and introduces a gap between the monomers which

in turn pushes VgrS into a conformation far wider than either the closed or open VgrG1 conformations (Figure 2A). This domain-swap has only been observed in VgrS setting it apart from previously described VgrGs (Figure S3A)[17,18,20,21].

To further probe the conformational states of VgrS we generated an AlphaFold3 model of trimeric VgrS ($VgrS_{AF}$) (Figure S3B). The predicted $VgrS_{AF}$ model resembles the closed conformation of VgrG1 more closely than the crystal structure of VgrS (r.m.s.d. of 4.206 $Å^2$ vs. 7.176 $Å^2$). Specifically, the domain swap residues observed in the VgrS crystal structure are modelled to match the anti-parallel β-sheet of VgrG1 and other VgrGs. The base of the $VgrS_{AF}$ model is also more compact than the crystal structure, resulting in a cavity of similar size to the closed conformation of VgrG1 (Figure 2A and Figure S3C). While this may represent training-set bias in AlphaFold3, it is possible that VgrS adopts both conformations represented by the crystal structure and the AlphaFold model. For VgrS, this conformational switch could be linked to conserved residues 356 to 366 (EHYEWPGDYFD) changing from an extended domain-swapped loop to a compact anti-parallel β-sheet similar to VgrG1 (Figure 2B, middle panel).

We also examined the B-factors in the structure, which can reveal regions of flexibility[45]. In VgrS, the highest B-factors were observed in the gp27 head domain at the domain-swap region and in the loop regions (Loop 4, 16, and 20) (Figure 2B, bottom panel and Figure S3D). This supports our hypothesis that VgrS may change conformation between a closed $VgrS_{AF}$ conformation and the open form observed in our structure. Additionally, a comparison with the VgrG1 crystal structure shows that in the open conformation the region where the domain swap occurs and the loop regions also exhibit high B-factors. The loop regions are thought to change conformation to interact with Hcps[18,20], suggesting that Hcp binding could play a role in influencing the open and closed conformations of VgrS.

**The molecular surface of VgrS reveals clues to effector loading**

Given that VgrS diverges within *Salmonella* serovars (Figure S1) and is structurally different from other VgrGs (Figures 1-2), we hypothesized that VgrS may have molecular features for *S.* Typhimurium specific effector loading. As such, we examined in detail the molecular surface properties of VgrS and its unique structural elements. These include

the short C-terminal tail of VgrS, the uniquely large inner cup of the gp27 head domain, and the sulfate coordination ring near the OB-fold.

The molecular surface of VgrS exhibits limited conservation within the C-terminal tail and gp27 head domain but is highly conserved in the neck region (Figure 3A). Notably, the base of the gp27 head domain shows no conservation especially within the loop regions that have been shown to interact with Hcp. However, the back of the hollow cup has some conservation and is interestingly a region of sulfate binding (Figure 3A and Figure S2B). Furthermore, this region leads into the highly conserved OB-fold motif followed by an anti-parallel β-sheet that is also the site of sulfate coordination. Specifically, conserved pairs of surface exposed residues Arg586/Lys597 and Glu601/609 bind sulfate (Figure 3A-B and Figure S2B). Given the high instance of sulfate coordination by conserved residues in VgrS, is it tempting to speculate that these regions may provide surfaces for effector loading that are ion and electrostatic dependent. This hypothesis is supported by that many effector-loading interactions are electrostatic[13,16]. However, effector loading at these sites will require experimental validation.

In line with an electrostatic mediated loading model, we analyzed the electrostatic surface of VgrS to gain further insight. Overall, VgrS is highly electronegative with patches of electropositive residues that show some residue conservation (Figure 3B). Notably, there is a high concentration of electronegative residues on the internal face within the gp27 head cup. Within this cavity, multiple His, Lys, and Arg residues coordinate sulfate ions, suggesting a potential functional role yet to be determined (Figure 3B, rotated view). In contrast, the uniquely short VgrS C-terminal extension contains several acidic residues. The extension runs downward alongside the spike, with the loop folding to interact with the β-prism formed by the same chain, so that residues D715, T718, D720, and P724 point away from the β-prism (Figure 3B, inset). It is likely, that VgrS recruits adaptors for effector loading through its unique electronegative extension given comparisons to other VgrGs[22,29,41].

Finally, we also examined VgrS for hydrophobic regions. Extensive hydrophobic interactions exist in the gp-27 head, the OB-fold neck domain, and the C-terminal spike. The spike region contains an internal repeating hydrophobic-polar-hydrophobic environment created by the side chains of residues pointing towards the centre of the β-

helix (Figure 3C). The first anti-parallel β-sheet (β23-β26) shows mainly hydrophobic residues (green) followed by a β-helix (β27-β32) which contains hydrophilic inward-facing side chains. The remaining β-helix including the second antiparallel β-sheet (β33-β35) contains hydrophobic residues. This repeating pattern is characteristic of the spike region reported in VgrG1 in *P. aeruginosa*[20]. However, overall VgrS does not have surface exposed hydrophobic patches further driving the hypothesis that effector loading is electrostatic mediated.

**VgrS conformation changes as a model to regulate Hcp binding**

In *S.* Typhimurium, three copies of the *hcp* gene are present. These include *hcp1* (STM0276) and *hcp2* (STM0279) both located within SPI-6, and a distally located *hcp3* that is not associated with SPI-6[46,47] The amino acid sequence identity between Hcp1-2 is nearly identical with only 10 amino acid differences between the two proteins (Figure 4A), yet the deletion of the respective genes shows different T6SS phenotypes[47]. This raises the question of how small sequence variations can lead to significant functional differences the T6SS.

To examine the molecular differences between Hcp1 and Hcp2, we utilized the previously solved crystal structures of Hcp1 (PDB: 5XHH) and Hcp2 (PDB: 5XEU), in conjunction with AlphaFold3 to model potential structural differences (Figure S4A). We modelled both proteins as hexamers, with the AlphaFold models closely resembling the Hcp2 crystal structure (r.m.s.d. 0.695 $Å^2$) (Figure S4B). Note, Hcp1 (5XHH is deposited as a monomer). Overall, the models were of high confidence and create a similar sized but smaller ring compared to other Hcp structures (Figure S4B) (~35 Å inner measurement) (PDB: 7YW0)[18]. Additionally, both Hcps have similar electrostatic surface properties (Figure 4A). Interestingly, this is in contrast to the T6SS from *Bacteroides fragilis* where VgrG and Hcp have complementary electrostatics[18]. Strikingly, most of the sequence differences between Hcp1 and Hcp2 were located on the interior leaflet of the hexameric rings (Figure 4A, middle and right). Some T6SS effectors have been shown to be transported through Hcp rings as a method of delivery[48]. Given this, the observed differences may represent a mechanism for effector selection, aligning with reported phenotypes[47].

Studies have shown that the flexible loops of Hcp interact with the dynamic loops at the base of the gp27 domain (Figure 2B, Figure 3A, and Figure S3D)[18]. Since the sequences of the extending loops of Hcp1 and Hcp2 are nearly identical, we hypothesized that they have a similar mechanism to bind VgrS. To observe how the loops of Hcp and VgrS may change conformation upon binding, we generated an AlphaFold3 model of the VgrS:Hcp2 complex (Figure 4B and Figure S4C). AlphaFold docked Hcp2 to the base of VgrS as expected and in the closed conformation. Namely, when comparing the domain swap region we see that AlphaFold chooses the closed form of the β-sheet for VgrS residues 356 to 366. Additionally, the VgrS:Hcp2 complex is modelled to have a change in the PAAR-binding site at the top of the spike reminiscent of the changes in observed in VgrG1 (Figure 4B, inset)[20]. However, the AlphaFold complex has a high predicted aligned error (PAE) (>30Å) in the loop regions of both proteins. This was not unexpected, as AlphaFold often exhibits high error for protein dynamics[49,50] (Figure S4C). Given the lack of model confidence at the VgrS:Hcp interface, all that can be inferred is that the loops in both VgrS and Hcp1-2 may undergo a conformational change to facilitate binding (Figure S4B bottom and Figure S4C).

Interestingly, regions in VgrS distant from the VgrS:Hcp interface also showed high pLDDT scores. This was unexpected as when modelled alone the VgrS model is of high confidence (Figure S3B). This further supports that there is a conformational relay between VgrS, Hcp, and likely the PAAR domain upon effector binding[18,20,49]. In the case of VgrS, the structural and modelling data highly suggests that the domain-swapped conformation observed in VgrS may act as an intermediary that relays a signal from the gp5 spike to the Hcp upon effector binding (Figure 4B, arrows).

## DISCUSSION

Understanding the T6SS is crucial for deciphering bacterial interactions with other species, especially in enteric bacteria known to cause severe disease. Here, we solve a structure of VgrS from *S. enterica* serovar Typhimurium. VgrS is a core T6SS component that serves as a modular platform for effector loading. Overall, the structure of VgrS diverges from other known VgrG proteins revealing molecular surfaces important for specific effector loading (Figure 1 and Figure 3). Additionally, VgrS contains a domain

swap in the gp27 head domain which results in a large open conformation not previously observed in any other VgrG protein (Figure 2). Moreover, the structural data in combination with modelling data indicates that VgrS may cycle between a closed conformation similar to known VgrG proteins and the conformation shown in our crystal structure (Figure 3 and Figure 4). This in turn likely serves as a signal relay across the length of VgrS. Specifically, to relay a signal between the PAAR binding site at the top of the gp5 spike to the base of the gp27 head for Hcp binding upon effector loading.

The VgrS crystal structure reveals an “open” conformation exhibited by the wide diameter of the gp27 cavity compared to other known VgrGs[17,18,20]. This open conformation features a flat spike to facilitate PAAR binding. This is opposite to the uneven surface seen in the open conformation of VgrG1, which is thought to inhibit PAAR binding. This difference in conformation suggests that the VgrS open conformation spike flat surface might allow for PAAR attachment. However, this conformation may also be due to crystal packing. As shown in Figure S2A, VgrS packs tip-to-tip at the PAAR binding surface which may influence its conformation.

The most prominent unique structural feature of VgrS is the domain swap within the gp27 head. This region is an ordered antiparallel β-sheet in all other known VgrG proteins (Figure 2). The domain swap between each monomer contributes to the open conformation observed in the crystal structure. Subsequently, the crystallographic B-factors (Figure S3D), AlphaFold modelling (Figure 4, Figure S3, and Figure S4) and a known PAAR-VgrG-Hcp complex[18] suggest that VgrS undergoes a significant conformational change upon effector binding. Namely, that the domain-swap region helps relay a conformational change across the VgrS structure in response to effector loading. Given this, we propose the following model in Figure 4C. VgrS starts in the open conformation similar to our crystal structure and is unable to bind Hcp. Upon loading of an effector via the C-terminal extension or a PAAR domain, VgrS changes to the closed conformation observed in other VgrG proteins. At this point, the gp27 base compresses and binds to either Hcp1 or Hcp2 that may already contain an effector within its ring. The VgrS:Hcp:effector complex can then nucleate assembly of the phage tail in the T6SS baseplate. This model is also supported by the observation that the binding of VgrG proteins to their cognate Hcp appears to act as a checkpoint, ensuring that effectors are

loaded before the subsequent polymerization of Hcp/TssBC sheath proteins and secretion out of the cell[25].

Previous findings suggest that multiple effectors can be secreted in a single T6SS firing event, indicating that VgrGs can be decorated with multiple effectors. However, the process of loading these effectors onto VgrG is still not fully understood. The electrostatic surface of VgrS reveals distinct patches of electronegative residues on both the external and internal sides of the gp27 domain (Figure 3). The external face, known to interact with the trafficking domains of effectors like the Rhs cage, is characterized by similar electrostatic interactions[29]. Additionally, our structural analysis of VgrS also suggests that effector loading may occur within the cavity of the gp27 head domain. Positioned at the bottom center of the trimer, this cavity forms a small triangular aperture with electrostatic residues that are accessible to the surrounding solvent (Figure 3B). This internal surface could be an effector loading site as the expansive ~52Å wide cavity is large enough to accommodate a globular protein. Indeed, previous Cyro-EM structures of VgrGs have shown potential cargo shuttled into the cavity of the gp27 domain[21].

Finally, the unique C-terminal tail of VgrS is also a likely site of *Salmonella* specific effector loading. This is supported by work showing that adaptors specifically load effectors onto the VgrG tail[22,29,41]. However, the adaptors required for this process have yet to be identified in *Salmonella.* Overall, the structure of VgrS reveals several potential sites of effector loading specific to *Salmonella* and provides a model of how effector loading may relay a signal for Hcp binding.

## METHODS

### Protein expression and purification of VgrS

VgrS from *S. enterica serovar* Typhimurium SL1344_0284 (Uniport accession number Q8ZRL1), codon optimized for *E. coli* was synthesized by Genscript in the vector pET22b. VgrS was placed between restriction sites NdeI and Xho1 with a N-terminal HRV-3C 6His-Tag for purification. A truncated version of this wild-type VgrS lacking the first 81 amino acids was created by Q5-mutagenesis (NewEngland Biolabs, NEB) to generate VgrS (residues 81-729) using primer pairs 5'-CAAGATGCTGTGAGCGCGATTGTG and 5'-

ATCGTCCGCGGTAACCGC. Primers were generated from Integrated DNA Technologies (IDT) and the construct was confirmed by sequencing (SickKids Toronto).

Once the expression construct was generated, the vector was transformed into *E.coli* BL21 (DE3) Gold cells which were grown in 50 mL Lysogeny Broth (LB) supplemented with 100 ug / mL ampicillin at 37 ºC overnight. The following morning, overnight cultures were transferred to 3L of fresh LB broth at a 1 and 100 dilution and grown at 37 ºC until an Optical Density (OD) of 0.6 at 600nm absorbance was reached. Protein expression was induced by the addition of 1 mM isopropyl β-d-1-thiogalactopyranoside (IPTG) and cells were further incubated for ~16 hours overnight at 20 ºC. After incubation, the cells were harvested by centrifugation at 4200 rpm for 30min and resuspended in 50 mL lysis buffer (50 mM Tris pH 8, 500 mM NaCl, 20 mM Imidazole). Before lysis, 1 mM PMSF and 10 mM MgCl2 were added to resuspended cells, along with a small amount of DNase. The cells were then lysed using an Emulsiflex-C3 High Pressure Homogenizer (Avestin) and centrifuged at 17,000 rpm (30,000xg) for 30 minutes at 4 ºC. The supernatant was run through a nickel-NTA agarose affinity chromatography gravity column (Goldbio) equilibrated by lysis buffer. The bound protein was washed with 5x column volumes of lysis buffer before being eluted by 1x column volumes of elution buffer (50 mM Tris pH 8, 500 mM NaCl, 500 mM imidazole). The collected elution was concentrated to 2 mL by centrifugation using a 30 kDa concentrator (Amnicon) and applied to a HiLoad 16/600 Superdex 200 column (GE Health Care) for size-exclusion chromatography (SEC) using a AKTA Pure (Cytivia). The column was equilibrated with gel filtration buffer (50 mM Tris pH 8, 250 mM NaCl, 1mM 2-Beta-mercaptoethanol). In instances removal of this 6His-tag was desired, VgrS (81-729) was digested O/N 4 ºC with 1/50 ratio of 3C-HRV protease and simultaneously dialyzed into gel filtration buffer. The reaction was concentrated and undigested material removed by a second pass over a nickel-NTA column before being further purified by gel-filtration. To confirm purity of all protein variants, fractions were run on a 15% SDS-PAGE gel and visualized with Coomassie Brilliant Blue. Selected fractions were concentrated and used for further crystallization experiments or flash frozen in liquid nitrogen for future use.

**Protein expression and purification of SciW and PLpro**

The PLpro construct was used as a positive control in our inductively-coupled mass-spectroscopy (ICP-MS) experiment has been described in previous studies[44]. The SciW construct used as a negative control in our ICP-MS was also from previous studies[23]. Both PLpro and SciW were expressed in *E. coli* BL21 (DE3) Gold cells which were grown in 50 mL Lysogeny Broth (LB) supplemented with 100 ug / mL ampicillin at 37 ºC overnight. Overnight cultures were transferred to 3 L of fresh LB broth at a 1 and 100 dilution and grown at 37 ºC until an Optical Density (OD) of 0.6 at 600nm absorbance was reached. 1 mM IPTG was added to induce protein expression and cells were further incubated for ~16 hours overnight at 20 ºC. After overnight incubation, cells were resuspended in lysis buffer (50 mm Tris pH 8.0, 500 mM NaCl, 20 mM imidazole) and lysed via an Emulsiflex-C3 High Pressure Homogenizer (Avestin). The cell lysate was clarified by centrifugation at 17,000 rpm (30,000xg) for 30 minutes at 4 ºC. Both SciW and PLpro were purified as described previously by nickel-NTA agarose affinity chromatography followed by size-exclusion chromatography (SEC) using a HiLoad 16/600 Superdex 75 column (GE Health Care) via an AKTA Pure (Cytivia). The final SEC buffer of both proteins was 50 mM Tris pH 8.0, 250 mM NaCl 1mM beta-mercaptoethanol (BME). The purity of all fractions was assessed using SDS-PAGE gel analysis and selected fractions were concentrated and flash frozen in liquid nitrogen for future IP-MS experiments.

**Protein crystallization of VgrS**

Crystallization of purified VgrS (81-729) with the 6His-tag was screened using commercially available screens (NeXtal, Molecular Dimensions) and an in-house Crystal Gryphon robot (Art Robbins Instruments). Conditions were screened at a protein concentration of 32 mg/mL, 18 mg/mL, and 8 mg/mL. VgrS crystals with the highest resolution of diffraction were obtained from 0.1M sodium acetate pH 5.0, 1.5 M ammonium sulfate in a 1:1 drop ratio using the sitting drop vapour diffusion method and incubated at 4 ºC.

**Data collection and refinement**

A VgrS data set was collected at the Canadian Light Source beamline CMCF-BM (08B1). VgrS crystals were cryo-protected by 25% glycerol. The reflections were integrated and scaled using XDS and merged using AIMLESS from the CCP4 program suite[51,52]. Data quality was analyzed with phenix.xtriage from the PHENIX package[53]. The structure of VgrG1 from *Pseudomonas aeruginosa* (PDB: 6H3L) was used to obtain the phases by molecular replacement using Phaser[54]. The initial model was then refined using phenix.refine from the PHENIX package, alternating with manual building using Coot[55,56] The stages of refinement were done using refmacat on the CCP4 cloud[57]. Note that the data set can be processed in $P6_322$ with a VgrS monomer as the asymmetric unit. The space group $C222_1$ was chosen to have the full biological unit of a VgrS trimer in the asymmetric unit. This choice was made for biochemical relevance as VgrS has domain swaps, differences between each monomer, and has a ligand coordination site constructed in part from each monomer. Model statistics are listed in Table 1. Molecular visualizations and graphics were generated using ChimeraX[58].

**Inductively coupled plasma mass-spectrometry (ICP-MS)**

Purified SciW, PLpro, and VgrS were dialyzed overnight at 4ºC into 10 mm Tris pH 7.5, 50 mM NaCl. 100 µL of each protein was added separately into 1 mL of mass-spectrometry grade nitric acid (Sigma) and 0.5 mL $H_2O_2$ (Sigma) for overnight digestion at room temperature. After digestion, milli Q water was used to dilute the digested solution to 10 mL. The same procedure was also done with 100 µL of dialysis buffer. The digested solutions were further diluted 10x for ICP-MS analysis. NIST 1643 was used as QA/QC (quality assurance/control) and indium (In) was used as an internal standard for the ICP-MS analysis. ICP-MS was carried out using an Agilent 8900 ICP-MS.

**DATA AVAILABILITY**

The X-ray structure of *Salmonella* Typhimurium str. LT2 VgrS has been deposited in the Protein Data Bank under accession code 9MLP

## SUPPORTING INFORMATION

This article contains supporting information.

## AUTHOR CONTRIBUTIONS

K.S., M.V.S., G.P conceived the study. All authors contributed to the experimental design. M.V.S and K. L. W. expressed, purified, and crystallized proteins. K.S., M.V.S. and G.P. solved and analyzed the crystal structure. K.S. performed structural modelling. K.S., M.V.S. and G.P. wrote the paper. All authors provided feedback on the manuscript.

## ACKNOWLEDGEMENTS

We would like to thank Wei Wang in the Department of Earth Sciences at the University of Manitoba for help with running and analysis of ICP-MS data. We thank Dr. Brian Mark for providing an expression plasmid for PLpro. We would also like to thank beamline CMCF-BM at the Canadian Light Source, which is supported by the Canada Foundation for Innovation (CFI), the Natural Sciences and Engineering Research Council (NSERC), the National Research Council (NRC), the Canadian Institutes of Health Research (CIHR), the Government of Saskatchewan.

## FUNDING AND ADDITIONAL INFORMATION

This work was supported by the Canadian Institutes of Health Research (CIHR) project grant PJT-180450 to G.P. and a Research Manitoba New Investigator operating grant to G.P. K.S. was supported through a National Science and Engineering Council (NSERC) postgraduate doctoral scholarship and M.V.S was supported by a Research Manitoba Graduate Studentship and a University of Manitoba Graduate Fellowship.

## CONFLICT OF INTEREST

The authors declare that they have no conflicts of interest with the contents of this article.

## REFERENCES


1. Mulder, D. T., Cooper, C. A. & Coombes, B. K. Type VI Secretion System-Associated Gene Clusters Contribute to Pathogenesis of Salmonella enterica Serovar Typhimurium. *Infect Immun* **80**, 1996–2007 (2012).
2. Sana, T. G. *et al. Salmonella* Typhimurium utilizes a T6SS-mediated antibacterial weapon to establish in the host gut. *Proc. Natl. Acad. Sci. U.S.A.* **113**, (2016).
3. Blondel, C. J., Amaya, F. A., Bustamante, P., Santiviago, C. A. & Pezoa, D. Identification and distribution of new candidate T6SS effectors encoded in Salmonella Pathogenicity Island 6. *Front. Microbiol.* **14**, 1252344 (2023).
4. Allsopp, L. P. & Bernal, P. Killing in the name of: T6SS structure and effector diversity. *Microbiology* **169**, (2023).
5. Blondel, C. J., Jiménez, J. C., Contreras, I. & Santiviago, C. A. Comparative genomic analysis uncovers 3 novel loci encoding type six secretion systems differentially distributed in Salmonella serotypes. *BMC Genomics* **10**, (2009).
6. Boyer, F., Fichant, G., Berthod, J., Vandenbrouck, Y. & Attree, I. Dissecting the bacterial type VI secretion system by a genome wide in silico analysis: what can be learned from available microbial genomic resources? *BMC Genomics* **10**, 104 (2009).
7. Aschtgen, M., Zoued, A., Lloubès, R., Journet, L. & Cascales, E. The C-tail anchored TssL subunit, an essential protein of the enteroaggregative *Escherichia coli* Sci-1 Type VI secretion system, is inserted by YidC. *MicrobiologyOpen* **1**, 71–82 (2012).
8. Brunet, Y. R., Zoued, A., Boyer, F., Douzi, B. & Cascales, E. The Type VI Secretion TssEFGK-VgrG Phage-Like Baseplate Is Recruited to the TssJLM Membrane

Complex via Multiple Contacts and Serves As Assembly Platform for Tail Tube/Sheath Polymerization. *PLoS Genet* **11**, e1005545 (2015).

9. Felisberto-Rodrigues, C. *et al.* Towards a Structural Comprehension of Bacterial Type VI Secretion Systems: Characterization of the TssJ-TssM Complex of an Escherichia coli Pathovar. *PLoS Pathog* **7**, e1002386 (2011).
10. Ma, L.-S., Lin, J.-S. & Lai, E.-M. An IcmF Family Protein, ImpL$_M$, Is an Integral Inner Membrane Protein Interacting with ImpK$_L$, and Its Walker A Motif Is Required for Type VI Secretion System-Mediated Hcp Secretion in *Agrobacterium tumefaciens*. *J Bacteriol* **191**, 4316–4329 (2009).
11. Nazarov, S. *et al.* Cryo- EM reconstruction of Type VI secretion system baseplate and sheath distal end. *The EMBO Journal* **37**, (2018).
12. Kudryashev, M. *et al.* Structure of the Type VI Secretion System Contractile Sheath. *Cell* **160**, 952–962 (2015).
13. Silverman, J. M. *et al.* Haemolysin Coregulated Protein Is an Exported Receptor and Chaperone of Type VI Secretion Substrates. *Molecular Cell* **51**, 584–593 (2013).
14. Stietz, M. S., Liang, X., Li, H., Zhang, X. & Dong, T. G. TssA-TssM-TagA interaction modulates type VI secretion system sheath-tube assembly in Vibrio cholerae. *Nat Commun* **11**, 5065 (2020).
15. Hernandez, R. E., Gallegos-Monterrosa, R. & Coulthurst, S. J. Type VI secretion system effector proteins: Effective weapons for bacterial competitiveness. *Cell Microbiol* **22**, e13241 (2020).
16. Flaugnatti, N. *et al.* Structural basis for loading and inhibition of a bacterial T6 SS phospholipase effector by the VgrG spike. *The EMBO Journal* **39**, e104129 (2020).

17. Günther, P. *et al.* Structure of a bacterial Rhs effector exported by the type VI secretion system. *PLoS Pathog* **18**, e1010182 (2022).
18. He, W. *et al.* Structure and assembly of type VI secretion system cargo delivery vehicle. *Cell Reports* **42**, 112781 (2023).
19. Jurėnas, D. *et al.* Mounting, structure and autocleavage of a type VI secretion-associated Rhs polymorphic toxin. *Nat Commun* **12**, 6998 (2021).
20. Spínola-Amilibia, M. *et al.* The structure of VgrG1 from *Pseudomonas aeruginosa* , the needle tip of the bacterial type VI secretion system. *Acta Crystallogr D Struct Biol* **72**, 22–33 (2016).
21. Yang, X. *et al.* Atomic Structure of the Francisella T6SS Central Spike Reveals a Unique α-Helical Lid and a Putative Cargo. *Structure* **27**, 1811-1819.e6 (2019).
22. Burkinshaw, B. J. *et al.* A type VI secretion system effector delivery mechanism dependent on PAAR and a chaperone–co-chaperone complex. *Nat Microbiol* **3**, 632–640 (2018).
23. Ahmad, S. *et al.* Structural basis for effector transmembrane domain recognition by type VI secretion system chaperones. *eLife* **9**, e62816 (2020).
24. Bondage, D. D., Lin, J.-S., Ma, L.-S., Kuo, C.-H. & Lai, E.-M. VgrG C terminus confers the type VI effector transport specificity and is required for binding with PAAR and adaptor–effector complex. *Proc. Natl. Acad. Sci. U.S.A.* **113**, (2016).
25. Wu, C. *et al.* Effector loading onto the VgrG carrier activates type VI secretion system assembly. *EMBO Reports* **21**, e47961 (2020).
26. Shneider, M. M. *et al.* PAAR-repeat proteins sharpen and diversify the type VI secretion system spike. *Nature* **500**, 350–353 (2013).

27. Zhang, Z. *et al.* PAAR Proteins Are Versatile Clips That Enrich the Antimicrobial Weapon Arsenals of Prokaryotes. *mSystems* **6**, e00953-21 (2021).
28. Lays, C., Tannier, E. & Henry, T. Francisella IglG protein and the DUF4280 proteins: PAAR-like proteins in non-canonical Type VI secretion systems? *Microb Cell* **3**, 576–578 (2016).
29. Colautti, J. *et al.* A widespread accessory protein family diversifies the effector repertoire of the type VI secretion system spike. *Nat Commun* **15**, 10108 (2024).
30. Lopez, J., Ly, P. M. & Feldman, M. F. The Tip of the VgrG Spike Is Essential to Functional Type VI Secretion System Assembly in *Acinetobacter baumannii*. *mBio* **11**, (2020).
31. Jurėnas, D. *et al. Salmonella* antibacterial Rhs polymorphic toxin inhibits translation through ADP-ribosylation of EF-Tu P-loop. *Nucleic Acids Research* **50**, 13114–13127 (2022).
32. Lorente Cobo, N. *et al.* Molecular characterization of the type VI secretion system effector Tlde1a reveals a structurally altered LD-transpeptidase fold. *Journal of Biological Chemistry* **298**, 102556 (2022).
33. Ong, S. Y., Ng, F. L., Siti Suriawati Badai, Yuryev, A., & Maqsudul Alam. Analysis and construction of pathogenicity island regulatory pathways in Salmonella enterica serovar Typhi. (2010) doi:10.2390/BIECOLL-JIB-2010-145.
34. Zhang, H. *et al.* Structure of the Type VI Effector-Immunity Complex (Tae4-Tai4) Provides Novel Insights into the Inhibition Mechanism of the Effector by Its Immunity Protein*. *Journal of Biological Chemistry* **288**, 5928–5939 (2013).

35. Quentin, D. *et al.* Mechanism of loading and translocation of type VI secretion system effector Tse6. *Nat Microbiol* **3**, 1142–1152 (2018).

36. Amaya, F. A. *et al.* Identification of Type VI Secretion Systems Effector Proteins That Contribute to Interbacterial Competition in Salmonella Dublin. *Front. Microbiol.* **13**, (2022).

37. Blondel, C. J. *et al.* The Type VI Secretion System Encoded in Salmonella Pathogenicity Island 19 Is Required for Salmonella enterica Serotype Gallinarum Survival within Infected Macrophages. *Infect Immun* **81**, 1207–1220 (2013).

38. Jones, D. T. & Cozzetto, D. DISOPRED3: precise disordered region predictions with annotated protein-binding activity. *Bioinformatics* **31**, 857–863 (2015).

39. Kelley, L. A., Mezulis, S., Yates, C. M., Wass, M. N. & Sternberg, M. J. E. The Phyre2 web portal for protein modeling, prediction and analysis. *Nat Protoc* **10**, 845–858 (2015).

40. Leiman, P. G. *et al.* Type VI secretion apparatus and phage tail-associated protein complexes share a common evolutionary origin. *Proc. Natl. Acad. Sci. U.S.A.* **106**, 4154–4159 (2009).

41. Berni, B., Soscia, C., Djermoun, S., Ize, B. & Bleves, S. A Type VI Secretion System Trans-Kingdom Effector Is Required for the Delivery of a Novel Antibacterial Toxin in Pseudomonas aeruginosa. *Front. Microbiol.* **10**, 1218 (2019).

42. Unterweger, D. *et al.* Chimeric adaptor proteins translocate diverse type VI secretion system effectors in *Vibrio cholerae*. *EMBO J* **34**, 2198–2210 (2015).

43. Bailey-Elkin, B. A. *et al.* Crystal structure of the Middle East respiratory syndrome coronavirus (MERS-CoV) papain-like protease bound to ubiquitin facilitates targeted

disruption of deubiquitinating activity to demonstrate its role in innate immune suppression. *J Biol Chem* **289**, 34667–34682 (2014).

44. Van Vliet, V. J. E. *et al.* Ubiquitin variants potently inhibit SARS-CoV-2 PLpro and viral replication via a novel site distal to the protease active site. *PLoS Pathog* **18**, e1011065 (2022).
45. Sun, Z., Liu, Q., Qu, G., Feng, Y. & Reetz, M. T. Utility of B-Factors in Protein Science: Interpreting Rigidity, Flexibility, and Internal Motion and Engineering Thermostability. *Chem. Rev.* **119**, 1626–1665 (2019).
46. Lin, Q. P., Gao, Z. Q., Geng, Z., Zhang, H. & Dong, Y. H. Crystal structure of the putative cytoplasmic protein STM0279 (Hcp2) from Salmonella typhimurium. *Acta Crystallogr F Struct Biol Commun* **73**, 463–468 (2017).
47. Wang, P., Dong, J.-F., Li, R.-Q., Li, L. & Zou, Q.-H. Roles of the Hcp family proteins in the pathogenicity of Salmonella typhimurium 14028s. *Virulence* **11**, 1716–1726 (2020).
48. Ma, J. *et al.* The Hcp proteins fused with diverse extended-toxin domains represent a novel pattern of antibacterial effectors in type VI secretion systems. *Virulence* **8**, 1189–1202 (2017).
49. Chakravarty, D. *et al.* AlphaFold predictions of fold-switched conformations are driven by structure memorization. *Nat Commun* **15**, 7296 (2024).
50. Penner, T. V. *et al.* Structural characterization of the Sel1-like repeat protein LceB from Legionella pneumophila. *Protein Sci* **33**, e4889 (2024).
51. Kabsch, W. *XDS*. *Acta Crystallogr D Biol Crystallogr* **66**, 125–132 (2010).

52. Winn, M. D. *et al.* Overview of the *CCP* 4 suite and current developments. *Acta Crystallogr D Biol Crystallogr* **67**, 235–242 (2011).

53. Adams, P. D. *et al. PHENIX*: a comprehensive Python-based system for macromolecular structure solution. *Acta Crystallogr D Biol Crystallogr* **66**, 213–221 (2010).

54. McCoy, A. J. *et al. Phaser* crystallographic software. *J Appl Crystallogr* **40**, 658–674 (2007).

55. Emsley, P., Lohkamp, B., Scott, W. G. & Cowtan, K. Features and development of *Coot*. *Acta Crystallogr D Biol Crystallogr* **66**, 486–501 (2010).

56. Painter, J. & Merritt, E. A. *TLSMD*web server for the generation of multi-group TLS models. *J Appl Crystallogr* **39**, 109–111 (2006).

57. Murshudov, G. N. *et al. REFMAC* 5 for the refinement of macromolecular crystal structures. *Acta Crystallogr D Biol Crystallogr* **67**, 355–367 (2011).

58. Pettersen, E. F. *et al.* UCSF CHIMERAX: Structure visualization for researchers, educators, and developers. *Protein Science* **30**, 70–82 (2021).

59. Yariv, B. *et al.* Using evolutionary data to make sense of macromolecules with a 'face-lifted' ConSurf. *Protein Sci* **32**, e4582 (2023).

## TABLES

**Table 1: X-ray data collection and structure refinement for VgrS.**

| **Data collection** | VgrS |
|---|---|
| Wavelength (Å) | 1.1802 |
| Space group | C 2 2 $2_1$ |
| **Cell dimensions** | |
| *a, b, c* (Å) | 121.147 209.917 470.971 |
| *α, β, γ* (°) | 90 90 90 |
| Resolution (Å) | 49.76 - 3.1 (3.15 - 3.1) |
| Total reflection | 736045 (35630) |
| Unique reflections | 108717 (5262) |
| CC(1/2) | 0.997 (0.511) |
| $R_{merge}$ | 0.212 (2.34) |
| $R_{pim}$ | 0.133 (1.474) |
| $I/\sigma I$ | 8.0 (0.9) |
| Completeness (%) | 99.9 (99.8) |
| Redundancy | 6.8 (6.8) |
| **Refinement** | |
| $R_{work}/R_{free}$ (%) | 19.8 / 22.8 |
| **Average B-factors (Å$^2$)** | 92.76 |
| Protein | 92.38 |
| Ligand | 156.03 |
| Water | 86.49 |
| **No. of atoms** | |
| Proteins | 14824 |
| Ligands | 91 |
| Water | 6 |
| **Rms deviations** | |
| Bond lengths (Å) | 0.0095 |

| | |
|---|---|
| Bond angles (°) | 2.1880 |
| **Ramachandran plot (%)** | |
| Total favored | 85.7 |
| Total allowed | 11.7 |
| Outliers | 2.6 |
| **PDB** | 9MLP |

## FIGURES AND LEGENDS

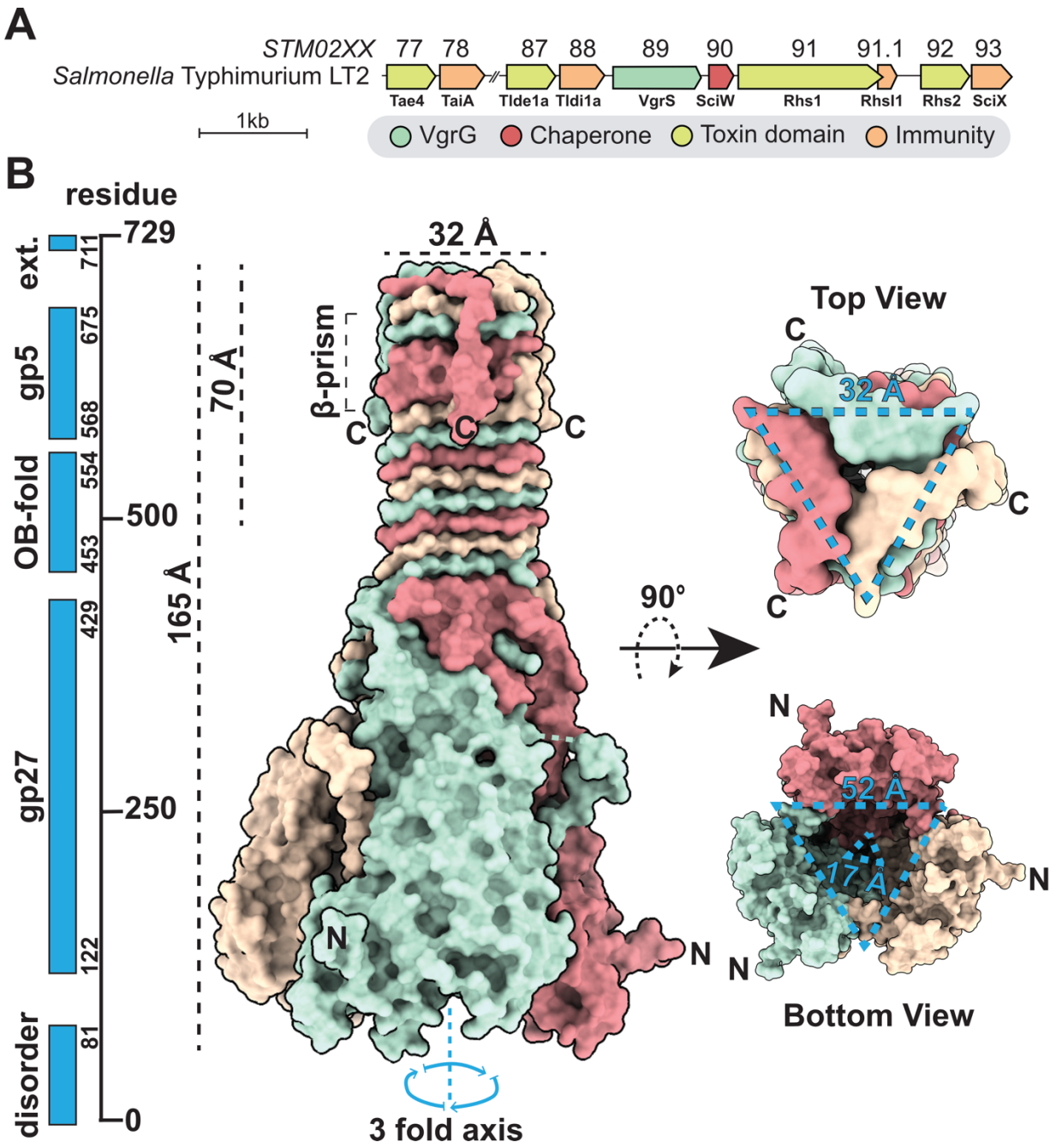


**Figure 1: X-ray crystal structure of VgrS. A)** The genes surrounding VgrS (STM0289) in *S.* Typhimurium LT2. **B)** Overall structural features of VgrS. Domain annotations for the VgrS sequence were generated using predictions from the CDD server and outlined by residue boundaries (left). The VgrS trimer is shown by surface representation with each monomer shown in a different color (middle). The top of the spike and base of the VgrS are shown and structural features measured (right).

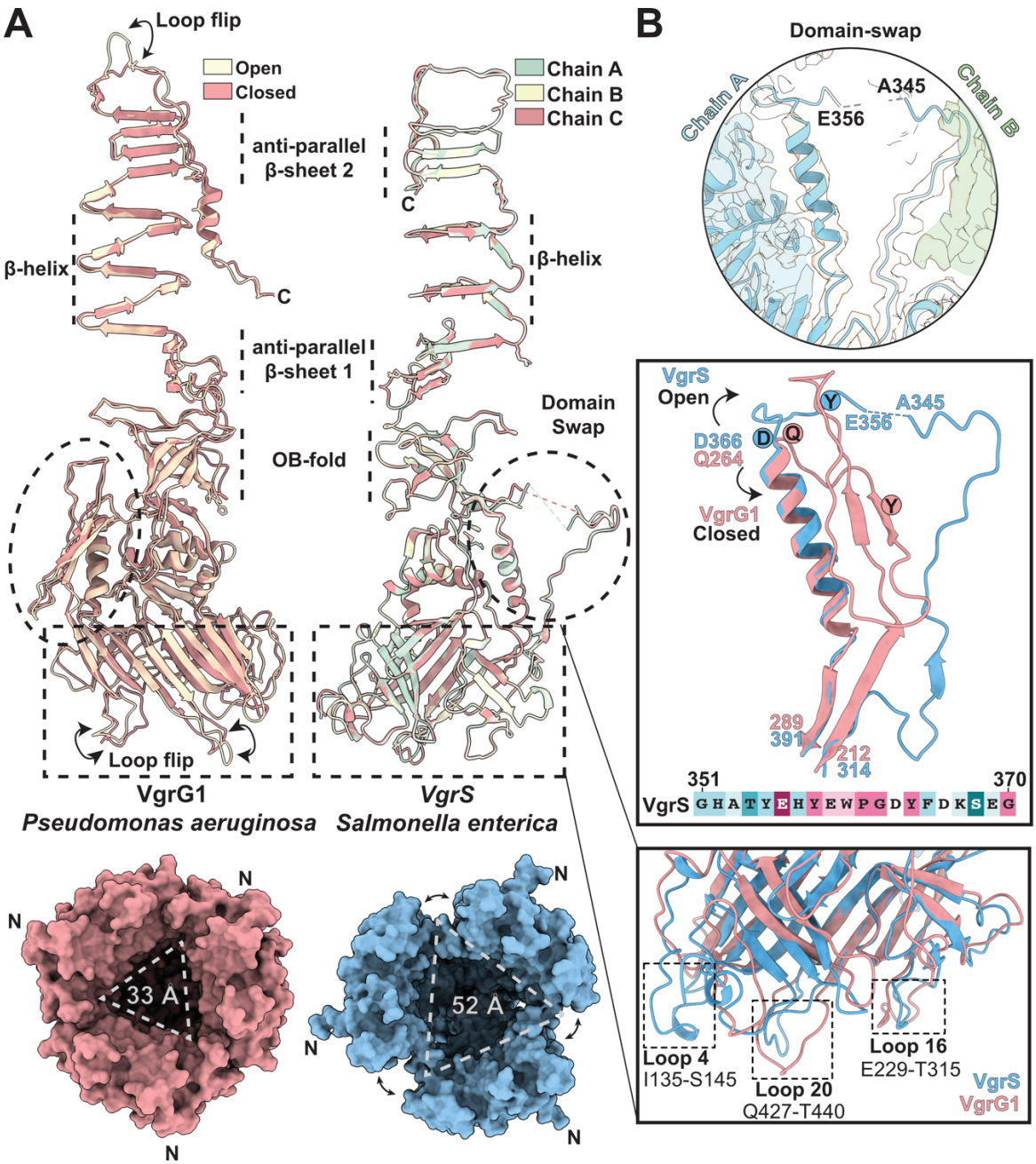


**Figure 2: The VgrS domain swap expands the gp27 head base to adopt an open conformation. A)** Comparative analysis of asymmetric units of VgrG1 and VgrS crystal structures. Top left: Overlayed chains of VgrS and VgrG1 in their "open" & "closed" conformation (PDB: 4UHV). Top right: Overlayed chains of each VgrS monomer. The size of the gp27 base is shown below each structure. **B)** Structure of the domain-swap region. Top: VgrS 2Fo-Fc density map illustrating the fit of the VgrS domain swap. Middle: Comparison of domain-swap region of VgrS with VgrG1 (PDB: 4UHV). VgrS is shown in

blue and VgrG1 in pink. Conserved residues in the region are highlighted using ConSurf[59] and relative positions shown on the structures. Bottom: Differences in the loop region conformations important for Hcp binding.

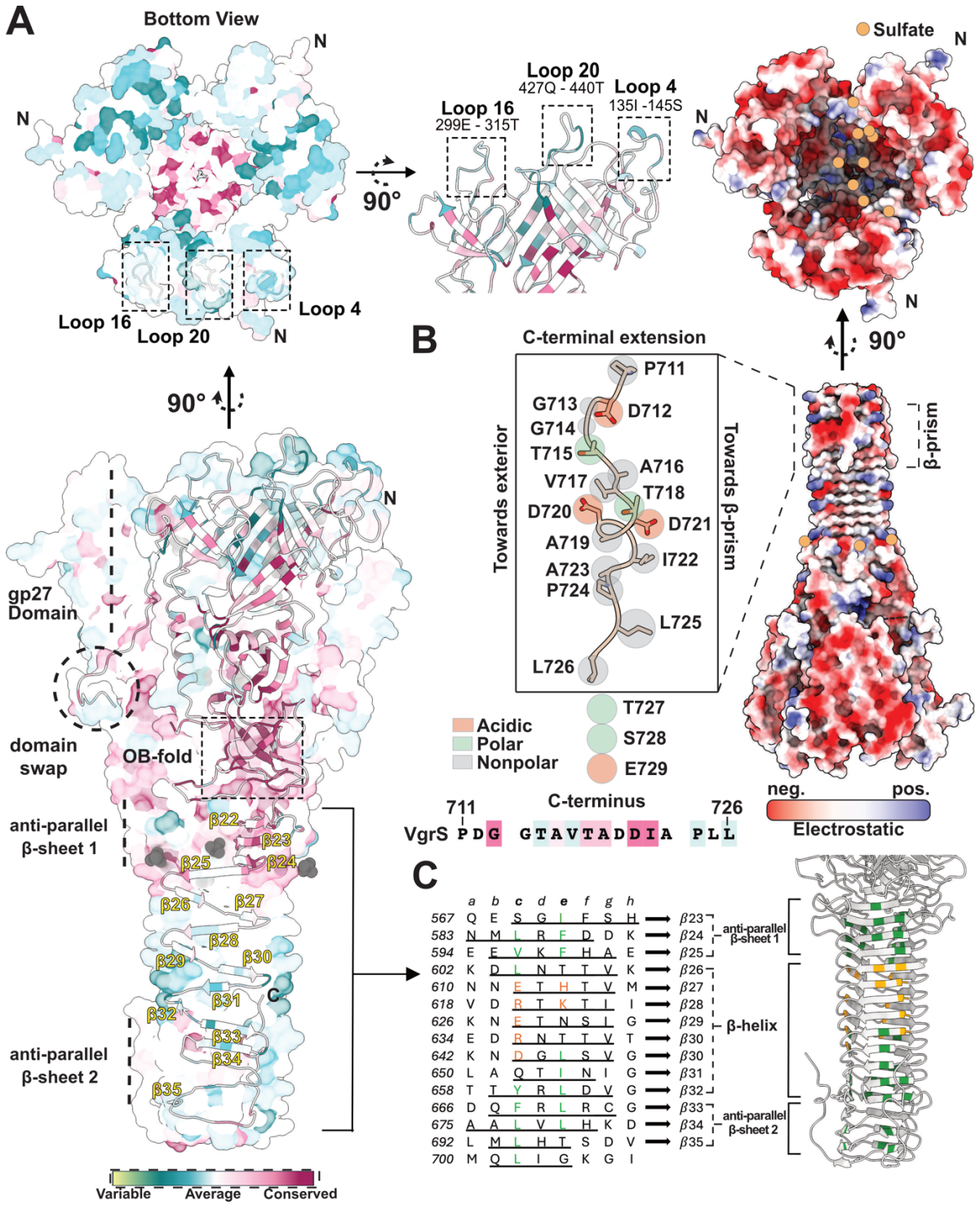


**Figure 3: Molecular surface properties of VgrS**. **A)** Surface conservation of VgrS as determined by the server ConSurf. Top: Molecular surface of the gp27 base with a rotated view of the Hcp binding loop regions showing they are unconserved. Bottom: Annotated molecular surface of VgrS. **B)** Relative electrostatic potential of the VgrS surface shown

in red (negative) and blue (positive). A rotation showing the surface of the gp27 base is also shown with positions of sulfate ligands indicated (orange). The inset is a zoom in of the C-terminal extension highlighting acidic (red), polar (green), and nonpolar (grey) residues. The orientation of the residues is indicated as pointing either toward or away from the β-prism. Residue conservation of the C-terminal tail is shown underneath **C)** Manual sequence alignment of the spike β-strands in VgrS (underlined). Left: Residues are coloured orange and green as hydrophobic and hydrophilic, respectively. Right: The C-terminal spike region (white) coloured to show the repeat hydrophobic (green) hydrophilic (orange) hydrophobic (green) pattern.

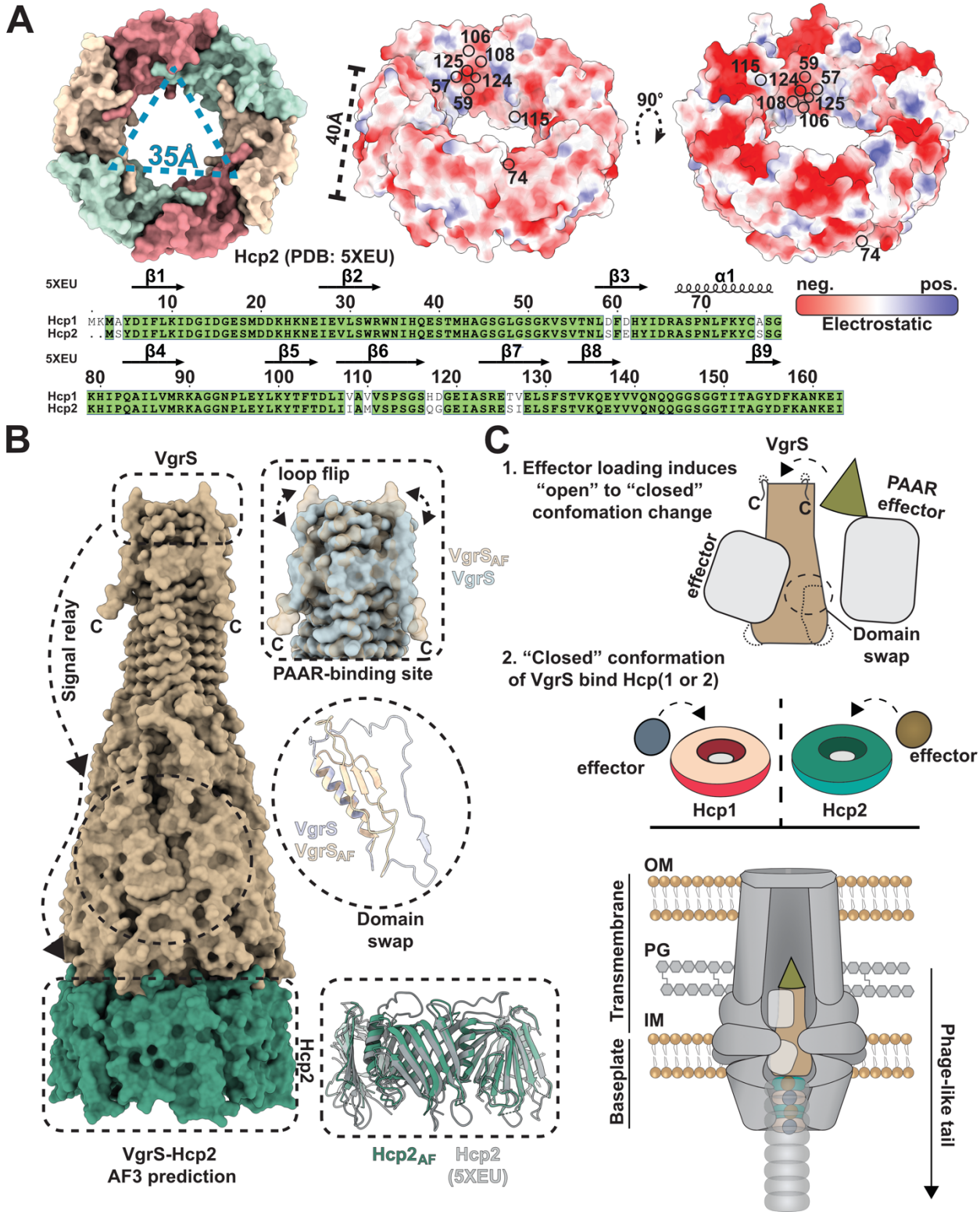


**Figure 4: Proposed mechanism of VgrS effector loading. A)** The general hexamic structure of Salmonella Hcp proteins is shown on the left, with the triangular dimensions of Hcp2 (PDB: 5XEU) were measured from the Tyr03-OH of every second chain. Middle

and right show electrostatic potential map of Hcp2 (PDB: 5XEU) and an AlphaFold hexamer of Hcp1, respectively. Bottom: Sequence alignment of Hcp1 and Hcp2, with the sequence differences highlighted on the electrostatic sufaces. **B)** Overall structure of the AlphaFold predicted VgrS:Hcp complex (left). Inset regions shown on the right highlight several conformational changes between the VgrS experimental structure, the predicted VgrS:Hcp complex, and Hcp bound or free. Arrows along VgrS indicate a potential signal relay from effector binding. **C)** Schematic diagram illustrating the proposed mechanism of VgrS conformational changes upon effector binding, and prior to being loaded onto the T6SS apparatus.